Catalysis Science & Technology

ROYAL SOCIETY OF CHEMISTRY

PAPER

View Article Online
View Journal | View Issue

Cite this: *Catal. Sci. Technol.*, 2025, 15, 486

The influence of size, metal loading and oxygen vacancies on the catalytic performance of Au/CeO_{2-x} in the sunlight-powered reverse water gas shift reaction†

Jordi Volders, [abc] Sander Bossier,[d] Sander Stulens,[abc] Bjorn Joos,[abc] Thomas Vranken, [abc] Francesc Sastre, [e] Jan D'Haen, [b] Ken Elen,[abc] Marcel A. Verheijen,[fg] Pegie Cool, [d] An Hardy, [abc] Pascal Buskens [*ae] and Marlies K. Van Bael [*abc]

This study reports the conversion of CO_2 and H_2 to CO and H_2O at low temperature and low pressure (up to 203 °C, p = 3.5 bar) using plasmonic Au/CeO_{2-x} photocatalysts, with mildly concentrated sunlight as the sole energy source (up to 9 kW m^{-2}). Systematic catalytic studies were carried out by varying the CeO_{2-x} particle size, Au particle size and loading, and the concentration of oxygen vacancies. Upon illumination, all Au/CeO_{2-x} catalysts showed a CO production of up to 2.6 ± 0.2 mmol CO per g_{Au} per h (104 ± 8 μmol CO per g_{cat} per h), while the supports without Au did not show any activity. We determined that both photothermal and non-thermal effects contribute to the light-driven reverse water-gas shift reaction catalysed by plasmonic Au/CeO_{2-x}. A photothermal contribution was found from the exponential relationship between the CO production and the solar irradiance. In the dark, all Au/CeO_{2-x} photocatalysts and supports without Au produced CH_4 instead of CO with ≥97% selectivity, indicating a significant non-thermal contribution in light. A linear dependence of catalytic activity on the accessible interface area between CeO_{2-x} and Au was found, which is in line with an associative formate-mediated reaction mechanism occurring at the metal–support interface. Tuning the V_O content through thermal treatments yielded decreased photocatalytic activity for oxidised samples, identifying them as pre-catalysts. The stability of the Au/CeO_{2-x} photocatalysts was evaluated, demonstrating that the catalytic performance was affected by adsorption of H_2O as a reaction product, which could be fully restored upon heating *in vacuo*.

Received 7th October 2024,
Accepted 22nd November 2024

DOI: 10.1039/d4cy01194e

rsc.li/catalysis

1 Introduction

To this day a large majority of the world's total energy supply is provided by fossil fuels, giving rise to extensive CO_2 emissions.[1] In view of the transition to a circular, net zero emission economy, CO_2 should not be seen as a waste product but as a feedstock for conversion into various carbon-based chemicals and fuels (carbon capture and utilisation, CCU).[2–8] For instance, syngas (a mixture of CO and H_2) could be produced from CO_2 and subsequently used to synthesise long-chain hydrocarbons *via* the Fischer–Tropsch process as well as various platform chemicals such as methanol, acetic acid and aldehydes.[9–15] Syngas can be obtained by CO_2 reduction in the reverse water gas shift (rWGS) reaction (eqn (1)).[13,16] The rWGS reaction is endothermic and competes with the exothermic methanation process (Sabatier reaction, eqn (2)). To predominantly produce CO, conventionally a high temperature of >600 °C is required.[13,17,18]

$$CO_2 + H_2 \rightleftharpoons CO + H_2O \quad \Delta H_{298K} = 41.2 \text{ kJ mol}^{-1} \qquad (1)$$

$$CO_2 + 4H_2 \rightleftharpoons CH_4 + 2H_2O \quad \Delta H_{298K} = -165.0 \text{ kJ mol}^{-1} \qquad (2)$$

[a] *Institute for Materials Research (imo-imomec), DESINe Group, Hasselt University, Agoralaan Building D, Diepenbeek 3590, Belgium. E-mail: marlies.vanbael@uhasselt.be*
[b] *IMOMEC Associated Laboratory, IMEC vzw, Wetenschapspark 1, Diepenbeek 3590, Belgium*
[c] *EnergyVille, Thor Park 8320, Genk 3600, Belgium*
[d] *Laboratory of Adsorption and Catalysis, Department of Chemistry, University of Antwerp, Universiteitsplein 1, Wilrijk B-2610, Belgium*
[e] *The Netherlands Organisation for Applied Scientific Research (TNO), Eindhoven, The Netherlands. E-mail: pascal.buskens@tno.nl*
[f] *Department of Applied Physics, Eindhoven University of Technology, Eindhoven 5600 MB, The Netherlands*
[g] *Eurofins Materials Science, High Tech Campus 11, Eindhoven 5656 AE, The Netherlands*

† Electronic supplementary information (ESI) available. See DOI: https://doi.org/10.1039/d4cy01194e

Photocatalysis, which utilises the energy of (sun)light to carry out the rWGS reaction at near-ambient conditions, is a promising alternative. Traditional photocatalysts are semiconducting materials, with ZnO and TiO_2 as common examples, in which light-generated electron–hole pairs drive reactions.[19–21] A challenge for these photocatalysts is that the majority of stable semiconductors have a bandgap energy exceeding 3 eV, which absorbs only UV wavelengths, excluding the majority of the solar spectrum. Possible ways to mediate this challenge are bandgap engineering and the use of cocatalysts.[21] Plasmonic nanoparticles (NPs), which are able to harvest a broad range of the solar spectrum, could act as cocatalysts in tandem with a semiconductor.[7,22–33] For metal NPs that are much smaller than the wavelength of incident light, the free electron gas of the metal exhibits an oscillation with a frequency equal to that of incident light, also known as the localised surface plasmon resonance (LSPR). This LSPR can activate reactants through several pathways. As a first effect, heat will be generated in the local vicinity of the plasmonic NP through the Joule effect, allowing for enhanced reaction kinetics. Secondly, light can be re-emitted at the same frequency as the incident light concentrated at specific positions at the NP surface, dependent on particle morphology. This effect is known as near-field enhancement which can strongly benefit photo-activated processes or generate additional charge carriers in the semiconductor. In a third pathway, the energy of the LSPR can be used to promote an electron to a higher energy level, referred to as a hot electron. When the plasmonic NP is in junction with a semiconductor, hot electrons can be injected into the conduction band over the Schottky barrier, increasing the charge carrier lifetime and thus their probability of participating in a reaction.[34–36] Finally, the conventional generation of electron–hole pairs in the semiconductor by UV excitation can also occur. The local heat generation is defined as a photothermal contribution, while the near-field enhancement, hot electron generation and injection and bandgap transition combined are referred to as non-thermal contributors.[35,37–41]

CeO_2 is a semiconductor with a face-centred cubic (FCC) fluorite crystal structure which is rarely fully stoichiometric and exhibits relatively large amounts of oxygen vacancies (V_Os) in its lattice. Every V_O results in two reduced Ce^{3+} sites while retaining the fluorite structure and can readily be reversed into stoichiometric CeO_2.[42–48] The V_Os allow for increased adsorption of CO_2 and have been shown to act as catalytic sites for rWGS on supported CeO_{2-x}, for both redox and associative reaction mechanisms. In the redox mechanism, the reaction occurs at a redox site of the catalyst, specifically at V_O sites of the support material as commonly catalytic metals for rWGS do not readily change valence states. In the associative mechanism, H_2 is dissociated at the catalytic metal and will react with CO_2 adsorbed on the support to result in carbon-containing intermediates (*e.g.* formates, carbonates), which are subsequently converted to CO.[18,49–56] Additionally, it has been demonstrated that deposition of metal NPs, *e.g.* Au, on the surface of CeO_{2-x} can significantly decrease the required temperature to form V_Os at the surface.[57–62] Due to these unique properties, CeO_{2-x} has been studied as a support[52,63–70] and photocatalyst in various applications like selective organic reactions,[71–75] hydrogen evolution reaction[76] and pollutant degradation.[77–81]

Several supported plasmonic materials have been investigated as photocatalysts for sunlight-driven rWGS: Ag,[82] Al,[83] Co,[84] Cu,[85,86] Fe,[87,88] Mo,[89] Ni,[90] Pt,[91–94] Pd (ref. 91, 95–97) and Ru.[98] In addition, Au has been widely reported as a plasmonic photocatalyst due to its strong LSPR effect and high selectivity towards rWGS. An overview of publications reporting supported Au plasmonic photocatalysts can be found in Table S1.†[25,27,30,85,99–103] Production rates are either normalized by the mass of the photocatalyst including the support, denoted as g_{cat}^{-1}, or by the mass of only the plasmonic metal (denoted as g_{Au}^{-1}). For supported Au plasmonic photocatalysts, no specific correlations between plasmonic Au size, loading and activity have been reported. In addition, the Au/CeO_{2-x} catalytic system for light-driven plasmonic rWGS is not yet fully understood: no correlation between photocatalytic activity and key structural properties has been reported. Upadhye *et al.* reported an Au/CeO_{2-x} photocatalyst with a CO production rate of 85.02 mmol g_{cat}^{-1} h^{-1}, which was a significant enhancement compared to the Au/Al_2O_3 photocatalyst with an insulating support. They also found the largest rate enhancement between dark and light experiments for Au/CeO_{2-x} compared to Au/TiO_2 and Au/Al_2O_3. For Au/TiO_2 they proposed a carboxyl-mediated associative mechanism at the metal–support interface where the LSPR assists in dissociation of the carboxyl intermediate or H_2O formation.[85] Lu *et al.* reported an Au/CeO_{2-x} photocatalyst with a CO production rate of approximately 7 mmol g_{cat}^{-1} h^{-1}; they attributed the activity difference between light and dark experimental conditions to the plasmon-associated dissociation of H_2 on the Au surface.[103]

In our study, we prepared and characterized a series of Au/CeO_{2-x} catalysts and focused on the influence of key structural properties of Au and CeO_{2-x}, more specifically particle size, Au loading and oxygen vacancies, on the catalytic performance of Au/CeO_{2-x} in the sunlight-powered rWGS reaction. By the obtained results, we gained insights on the impact of photothermal heating and the nature of non-thermal effects contributing to the reaction.

2 Results and discussion

2.1 Characterisation

2.1.1 Hydrothermal synthesis of CeO_{2-x}. Two distinct CeO_{2-x} support particle sizes were synthesised using a hydrothermal (HT) method as described in the experimental methods in the ESI,† namely large (L-HT) and small (S-HT) particles. In summary, $Ce(NO_3)_3{\cdot}6H_2O$ and polyvinylpyrrolidone (PVP) were dissolved in an ethanol : water mixture (1 : 2 for L-HT and 3 : 1 for S-HT), then transferred to a Teflon-lined autoclave and left in an oven at 160 °C (20 h for L-HT, 14 h for S-HT).

Finally, the solvent was evaporated in ambient air and a powder was obtained. A sample list with a summary of characterisation is available in Table S2.† Particle sizing with dynamic light scattering (DLS) (Fig. S1c and h†) of the as-synthesised dispersion yielded a particle size of 376 ± 6 nm and 53 ± 3 nm for L-HT and S-HT, respectively, with a confidence interval of 98%. Particle size distributions from transmission electron microscopy (TEM) analyses (Fig. S1a, b, d and e†) yielded particle sizes of 200 ± 7 nm and 35.5 ± 0.7 nm for L-HT and S-HT, respectively, with a confidence interval of 98%. The hydrodynamic diameter obtained by DLS is likely a larger value than particle sizes found in TEM analysis due to the presence of the electric double layer, organic residuals and agglomeration. Thermogravimetric analysis (TGA) was performed (Fig. S1i†) and a weight loss of 68% and 72% was observed for L-HT and S-HT below 450 °C, indicating a large amount of organic material still present in the powders. This was confirmed by attenuated total reflection Fourier-transform infrared (ATR-FTIR) spectroscopy (Fig. S1g†), where characteristic CH and CH_2 stretch vibrations (around 2900 cm^{-1}) originating from the PVP surfactant are present in both L-HT and S-HT samples. X-ray diffraction (XRD) (Fig. 1c) analyses of both samples exhibited the characteristic fluorite structure of CeO_2 (JCPDS 65-5923). Additional peaks can be attributed to the LaB_6 internal standard (JCPDS 06-0401) which was added as a reference for accurate peak position determination.

2.1.2 Calcination of CeO_{2-x}. To remove organic and nitrate impurities from CeO_{2-x}, L-HT and S-HT the samples were calcined in dry air at 400 °C to result in CeO_{2-x} powders with large (L) and small (S) particle sizes. XRD (Fig. 1c) shows that the CeO_2 fluorite crystal structure is retained for both L and S, with increased peak intensity compared to L-HT and S-HT, which indicates an increase in crystallinity. Crystallite sizes calculated using Scherrer's equation can be considered identical for both samples, *viz.* 12 nm and 13 nm for L and S, respectively. Size analyses based on TEM images yielded superstructure sizes, consisting of aggregated smaller crystallites of 196 ± 13 nm and 37 ± 2 nm for L and S, respectively, with a 98% confidence interval (Fig. 1a–d). Calcination had no significant impact on the particle size distribution. Brunauer–Emmett–Teller (BET) analyses were performed on N_2 physisorption isotherms (Fig. S1j†) to study the specific surface area of the samples and BET surface areas of 81 $m^2\ g^{-1}$ and 115 $m^2\ g^{-1}$ were found for L and S, respectively. The variance in specific surface area is in line with expectations due to the difference in particle size. Thus, it can be concluded that for L and S the crystallite sizes are equivalent although they are assembled in differently sized superstructures, meaning that differences between L and S samples could solely be attributed to the differences in surface area. ATR-FTIR (Fig. S1g†) shows that stretching vibrations of organic compounds can no longer be observed for L and S samples. Following peak attributions by Li *et al.*[104] (Table S3†), the characteristic CeO_2 vibrations and vibrations of bidentate and unidentate carbonates are observed for both L and S samples as well as adsorbed H_2O.

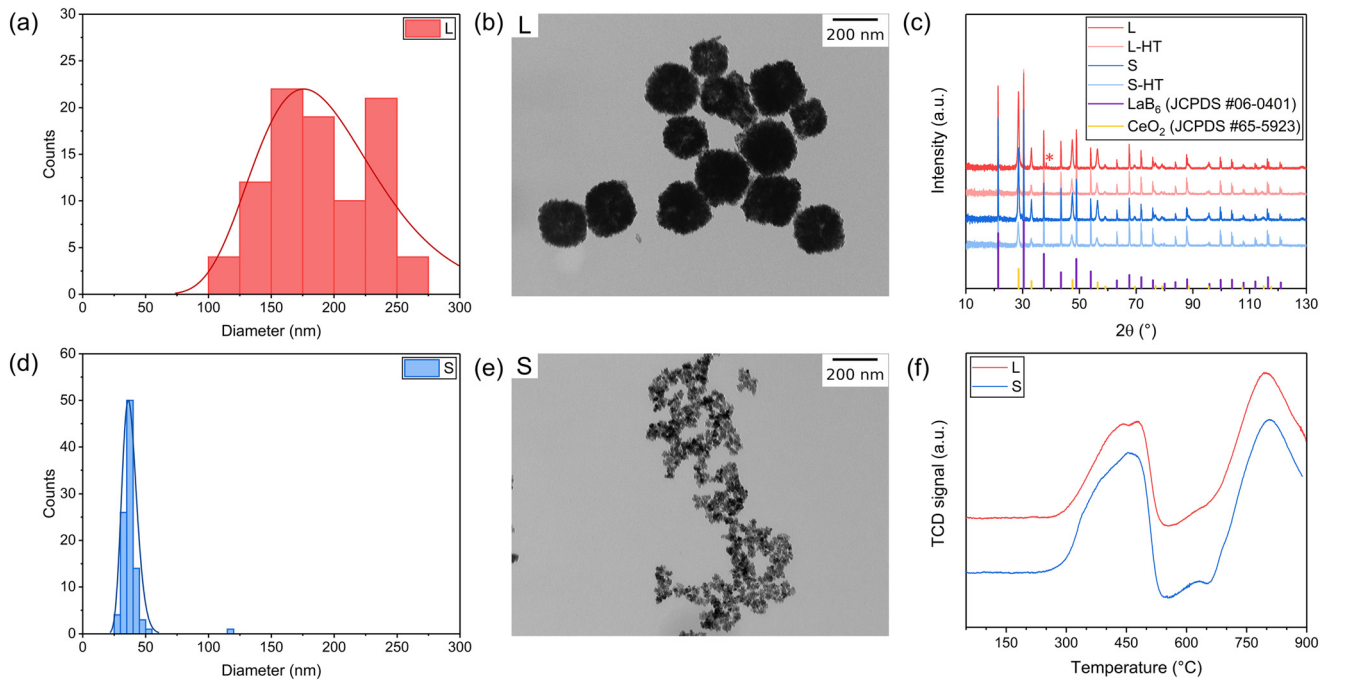

Fig. 1 (a) Particle size distributions of L CeO_{2-x} support from TEM analysis with lognormal fit. (b) Representative TEM image of L CeO_{2-x} particles. (c) XRD diffractograms of L-HT, S-HT, L and S CeO_{2-x} particles with LaB_6 as internal standard. Intensity is normalised on the wt% of sample in the sample/LaB_6 mixture. Graphs have been stacked for visual clarity. The * denotes an impurity peak of the Al sample stage in the L sample. (d) Particle size distributions of S CeO_{2-x} support from TEM analysis with lognormal fit. (e) Representative TEM image of S CeO_{2-x} particles. (f) H_2-TPR profiles of S and L CeO_{2-x} particles; graphs have been stacked for visual clarity.

Additional vibrations of bridged carbonates are found for the S sample, which are not present in the L sample. Diffuse reflectance UV-vis spectroscopy was performed in order to study the optical properties of the CeO_{2-x} samples (Fig. 2c). One absorption band around 400 nm is observed for both L and S samples, attributed to the bandgap of CeO_{2-x}. Tauc analysis (Fig. S1h†) was performed on the UV-vis spectra to obtain the bandgap energy, resulting in 3.26 ± 0.03 eV for L and 3.15 ± 0.03 eV for S samples, with a 98% confidence interval. The redshift in bandgap energy for the S sample may be the result of a larger amount of V_Os due to an increase in surface area. Raman spectroscopy (Fig. S2a and b†) shows the F_{2g} mode of the fluorite structure at 462.8 cm^{-1} and 462.2 cm^{-1} for L and S, respectively. Transverse (TO) and longitudinal optical (2LO) overtones are also observable for both samples at around 260 cm^{-1} and 1200 cm^{-1}, respectively. Additionally, a small peak, often referred to as the defect band (D) which can be related to V_Os, is observable around 600 cm^{-1}, with no significant difference between L and S samples.[105] Finally, a small peak is observable at around 725 cm^{-1} which could be attributed to adsorption of oxygen species. The reduction behaviour of the ceria powders was investigated by hydrogen temperature-programmed reduction (H_2-TPR) measurements (Fig. 1f and Table S4†). Two reduction domains were identified for both samples. The first reduction domain at 300–500 °C can be attributed to formation of V_Os at the CeO_{2-x} surface, consisting of two peaks: around 350 °C, reduction at the particle surface, then at around 450 °C, formation of V_Os at the sub-surface.[106] A second reduction domain starting at about 700 °C is attributed to the formation of V_Os in the bulk of CeO_{2-x}. Integration of peaks below 500 °C shows 391 μmol g^{-1} H_2 uptake (41.8% of total H_2 uptake at the CeO_{2-x} surface) and 480 μmol g^{-1} H_2 uptake (55.2% of total H_2 uptake at the CeO_{2-x} surface) for L and S, respectively, which aligns with the BET results. Thus, TPR results indicate that a larger quantity of V_Os at the surface can be formed for S CeO_{2-x} due to an increased surface area.

2.1.3 Au deposition on CeO_{2-x}. Au was deposited on L and S CeO_{2-x} using a deposition–precipitation method with chemical reduction as described in the experimental methods in the ESI,† resulting in 4Au/L and 4Au/S samples, respectively. A sample list with a summary of characterisation is available in Table S2.† The deposited Au content was quantified with inductively coupled plasma-optical emission spectroscopy (ICP-OES), resulting in a loading of 4.0 ± 0.8 wt% Au and 3.8 ± 0.9 wt% Au for 4Au/L and 4Au/S, respectively, with a confidence interval of 95%. High-angle annular dark-field scanning TEM (HAADF-STEM) analyses (Fig. 2a and e) were performed to study the size and morphology of the deposited Au nanoparticles. The HAADF contrast between Au and CeO_{2-x} could not be used to distinguish the locations and dimensions of the Au NPs, as thickness variations of the CeO_{2-x} particles themselves lead to similar contrast differences to those between Au and CeO_{2-x}.

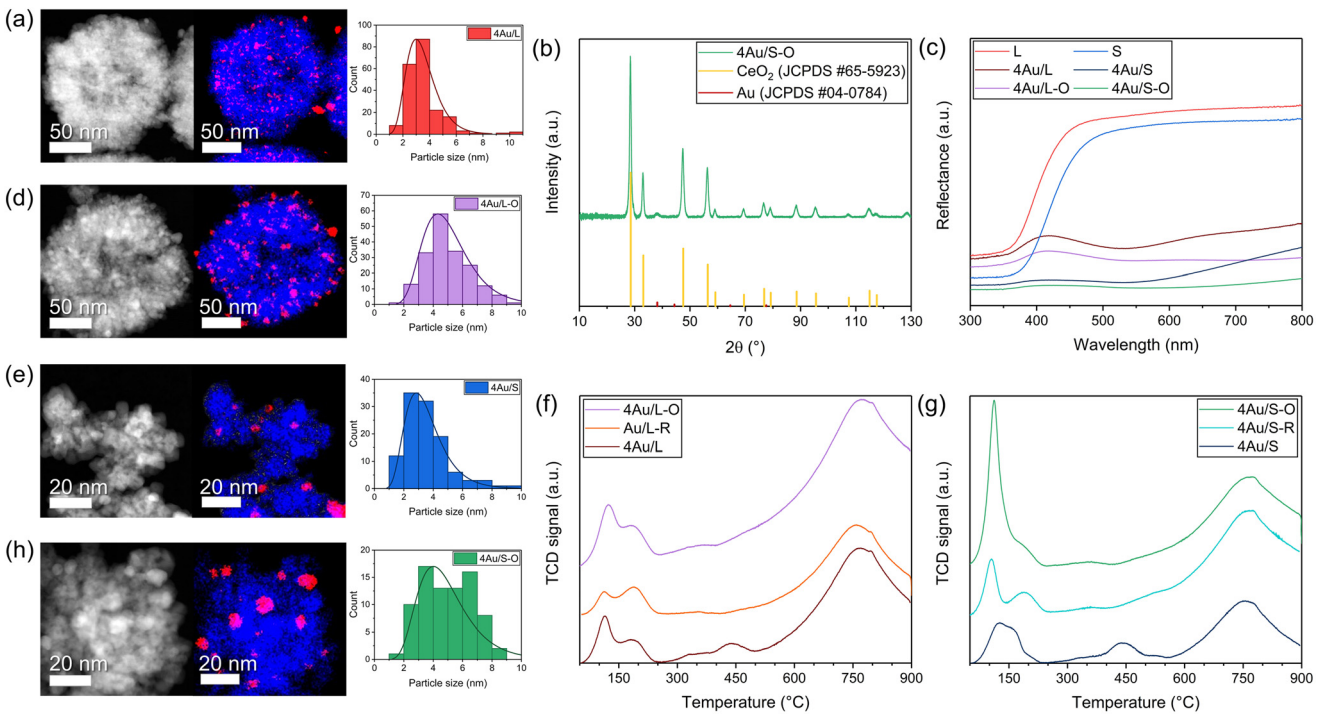

Fig. 2 Representative HAADF-STEM image, EDX mapping in STEM mode and Au particle size distribution from TEM analysis with lognormal fit of (a) 4Au/L, (d) 4Au/L-O, (e) 4Au/S and (h) 4Au/S-O Au/CeO_{2-x} samples. CeO_{2-x} is coloured blue and Au is coloured red in EDX mapping, lower magnification shown for (a) and (d) to illustrate CeO_{2-x} size particle difference. (b) XRD diffractogram of 4Au/S-O. (c) Reflective diffuse UV-vis spectra of L, 4Au/L, 4Au/L-O, S, 4Au/S and 4Au/S-O samples; graphs have been stacked for visual clarity. H_2-TPR profiles of (f) 4Au/L-O, 4Au/L-R and 4Au/L and (g) 4Au/S-O, 4Au/S-R and 4Au/S; graphs have been stacked for visual clarity.

Therefore, energy-dispersive X-ray (EDX) spectroscopy mappings were performed in STEM mode for all samples to unambiguously identify the Au nanoparticles. Au particle sizes of 3.5 ± 0.2 nm and 3.6 ± 0.3 nm were determined for 4Au/L and 4Au/S, respectively. XRD (Fig. S3a and b†) was performed on the 4Au/L and 4Au/S samples which revealed that the fluorite crystal structure of CeO_2 was retained while Au could not be observed, likely due to the small Au NP size and a low diffraction volume of present Au. Diffuse reflectance UV-vis spectroscopy (Fig. 2c) was performed, and in addition to the CeO_2 bandgap, the characteristic plasmonic absorption band of Au was observed with a minimum reflectance at 531 nm and 530 nm for 4Au/L and 4Au/S, respectively. Tauc analysis could not be performed on spectra of Au/CeO_2 samples due to spectroscopic overlap of the Au plasmonic absorption band with the CeO_2 bandgap. Raman spectroscopy (Fig. S2a and b†) was performed with a 785 nm laser source instead of a 532 nm laser source, but a large loss in peak intensity was observed due to strong visible light self-absorption in the sample, severely reducing the detection limit. The characteristic F_{2g} peak can be observed at 460.5 cm^{-1} and 461.7 cm^{-1} for Au/L and Au/S, respectively, which is a slight redshift compared to L and S. The TO peak can still be observed around 265 cm^{-1} and the D band consists of two components: one around 550 cm^{-1} and one around 600 cm^{-1}. The former has been reported to be specifically linked to the presence of V_Os.[105,107] However, attempts to determine V_O content in the Au/CeO_{2-x} did not yield dependable results due to variations between samples and the aforementioned strong self-absorption. In H_2-TPR (Fig. 2f and g and Table S4†) the reduction of bulk CeO_{2-x} remained unchanged, and the position of the sub-surface reduction peak at 450 °C remains for both Au/L and Au/S. However, the formation temperature of V_Os at the particle surface is drastically lowered by the addition of Au at <150 °C; a small peak remains at 350 °C, likely due to some inhomogeneity where surface CeO_2 is not located close to Au. The peak at 150–250 °C can similarly be attributed to formation of sub-surface V_Os which is lowered due to addition of Au. Furthermore, integration of the peaks below 500 °C (Table S4†) shows that both Au/L and Au/S have significantly less H_2 uptake, 18.7% and 31.7% respectively, for the formation of surface V_Os compared to L (41.8%) and S (55.2%), indicating that a significant number of V_Os is already present in the catalysts upon Au deposition. Additionally, a significantly larger number of sub-surface V_Os are also present in 4Au/L (60 μmol H_2 per g surface uptake and 86 μmol H_2 per g, 0.27 ratio) compared to L (83 μmol H_2 per g surface uptake and 308 μmol H_2 per g, 0.69 ratio), indicating that Au deposition has a significant impact on sub-surface reduction.

2.1.4 Thermal treatment of Au/CeO_{2-x}. In order to independently study the impact of both CeO_{2-x} size and V_Os in the Au/CeO_{2-x} catalysts, catalyst materials were thermally treated for 2 h at 500 °C in dry air to minimise V_O content, which resulted in 4Au/L-O and 4Au/S-O from 4Au/L and 4Au/S, respectively. Additionally, the 4Au/L and 4Au/S catalysts were thermally treated for 2 h at 500 °C in 5% H_2 in N_2 in order to increase V_O content and study its impact on catalysis, resulting in 4Au/L-R and 4Au/S-R, respectively. A sample list with a summary of characterisation is available in Table S2.† HAADF-STEM analyses (Fig. 2d and h) were performed to study the size and morphology of the deposited Au. Au particle sizes of 5.1 ± 0.3 nm and 4.9 ± 0.4 nm were determined for 4Au/L-O and 4Au/S-O, respectively. Particle growth of Au NPs occurred during thermal treatment, which resulted in larger average sizes compared to as-synthesised 4Au/L and 4Au/S. This was not the case for 4Au/L-R and 4Au/S-R (Fig. S4c and d†), where no significant change in particle size was observed at 3.0 ± 0.3 nm and 3.8 ± 0.4 nm, respectively. XRD (Fig. 2b) was performed for 4Au/L-O without an internal standard. In addition to diffraction peaks of CeO_2 (JCPDS 65-5923), one characteristic Au (JCPDS 04-0784) diffraction peak at a 2θ value of 38.19°, corresponding to *hkl* values of (111), could be observed. Further peaks were not observable due to low intensity and the Scherrer method could not be used to estimate the Au crystallite size due to low peak intensity. For 4Au/L-O, 4Au/S-O, 4Au/L-R and 4Au/S-R with an internal standard (LaB_6) no significant changes were observable compared to 4Au/L and 4Au/S. Diffuse reflectance UV-vis spectroscopy (Fig. 2c) was performed and the plasmonic absorption band of Au was observed slightly redshifted to 547 nm and 568 nm for 4Au/L-O and 4Au/S-O, respectively. For the 4Au/L-O sample an additional shoulder could be observed at 695 nm. A small redshift is expected due to particle growth, while the strongly redshifted shoulder is a possible result of partial agglomeration of Au. No significant change in plasmon absorption bands after reductive thermal treatment were observed for 4Au/L-R and Au/S-R (Fig. S4b†). The catalysts' specific surface area was investigated with BET (Fig. S1j†), resulting in BET surface areas of 62 $m^2\ g^{-1}$, 86 $m^2\ g^{-1}$, 59 $m^2\ g^{-1}$ and 84 $m^2\ g^{-1}$ for 4Au/L-O, 4Au/S-O, 4Au/L-R and 4Au/S-R, respectively. A decrease of specific surface area for all samples compared to L (81 $m^2\ g^{-1}$) and S (115 $m^2\ g^{-1}$) is likely a result of the Au deposition process and subsequent thermal treatment. The significant difference for the Au/CeO_{2-x} with large and small CeO_{2-x} remained. Raman analyses (Fig. S2a and b†) yielded F_{2g} positions of 459.2 cm^{-1}, 460.8 cm^{-1}, 460.7 cm^{-1} and 461.3 cm^{-1} for 4Au/L-O, 4Au/S-O, 4Au/L-R and 4Au/S-R, respectively. D positions at around 550 cm^{-1} and 600 cm^{-1} were observed as well, and similar to 4Au/L and 4Au/S, no assessment of V_Os could be made from these results. H_2-TPR results (Fig. 2f and g and Table S4†) indicate the same reduction peak for all samples above 700 °C, attributed to the bulk V_O formation. The reduction peak at around 450 °C from sub-surface V_O formation is absent in all samples, fully lowering this peak to 200 °C. This was possibly due to some surface restructuring during thermal treatments, which could not be reached during the mild conditions of the Au deposition. Furthermore, 4Au/L-O (25.7% surface H_2 uptake) and 4Au/S-O (30.6% surface H_2 uptake) show a very intense reduction peak at 125 °C compared to 4Au/L-R (16.0% surface H_2 uptake) and 4Au/S-R (20.6% surface H_2 uptake), integrations of which

(Table S4†) indicate that the thermal treatments are adequate to tune V_Os in the catalysts.

2.1.5 Au size variation in Au/CeO_{2-x}. To study the impact of the plasmonic Au on the light-driven rWGS reaction, Au loadings of 0.4 wt%, 1.5 wt% and 6.0 wt% Au were deposited on the S CeO_{2-x} sample using two different deposition–precipitation methods, producing samples denoted 0.4Au/S, 1.5Au/S and 6Au/S. An alternative deposition–precipitation method for the synthesis of 0.4Au/S was utilised in order to achieve a smaller Au particle size (<2 nm), which is below the minimum that can be achieved with the synthetic method using urea (3.5 nm). No further thermal treatment was performed so as to not influence V_Os, as the same S CeO_{2-x} sample was used as support material. A sample list with a summary of characterisation is available in Table S2.† The Au content for each sample was determined using ICP-AES, resulting in 0.41 ± 0.02 wt% for 0.4Au/S, 1.57 ± 0.08 wt% for 1.5Au/S, and 5.75 ± 0.4 wt% for 6Au/S, with a confidence interval of 95%. HAADF-STEM analysis (Fig. 3a and b) was carried out to study the size and morphology of the deposited Au. Equivalent Au particle sizes of 3.9 ± 0.3 nm and 3.5 ± 0.3 nm were determined for 1.5Au/S and 6Au/S, respectively. No individual Au particles could be identified for construction of a size distribution. This was due not only to the aforementioned poor contrast but also to the low loading and very small Au particle size (<2 nm) of the 0.4Au/S sample (Fig. S4a†), requiring high spatial resolution EDX mappings with long acquisition times, leading to time-consuming mappings in which no particles appeared to be present in the scanned areas. However, as this synthesis is adapted from a work previously reported by our group where better contrast between Au and TiO_2 allowed for particle size determination, an Au particle size of 1.6–1.7 nm is expected.[25,27] Diffuse reflectance UV-vis spectroscopy (Fig. 3c) was performed in which the CeO_2 bandgap was observed in the near-UV region (<400 nm) and the LSPR peak of Au was observed with a minimum reflectance at 533 nm, 532 nm and 526 nm for 0.4Au/S, 1.5Au/S and 6Au/S, respectively. These values are comparable with the observations above for 4Au/S and 4Au/L. XRD (Fig. S3c†) was performed on 0.4Au/S, 1.5 Au/S and 6Au/S and no significant differences could be observed compared to 4Au/S.

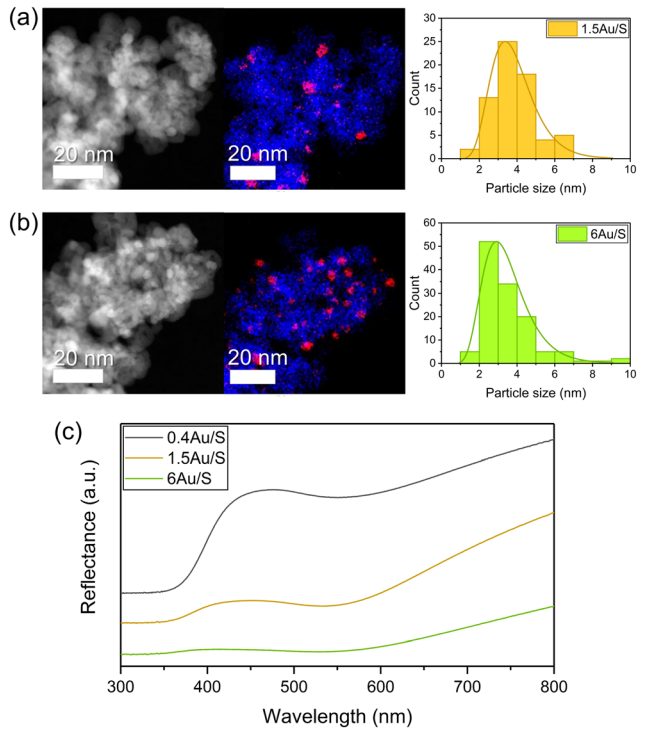

Fig. 3 Representative HAADF-STEM image, EDX mapping in STEM mode and Au particle size distribution from TEM analysis with lognormal fit of (a) 1.5Au/S and (b) 6Au/S. CeO_{2-x} is coloured blue and Au is coloured red in EDX mapping. (c) Diffuse reflective UV-vis spectra of 0.4Au/S, 1.5Au/S and 6Au/S; graphs have been stacked for visual clarity.

2.2 Catalysis

2.2.1 Irradiance variation. The catalytic activity of Au/CeO_{2-x} photocatalysts for the light-driven rWGS reaction was investigated using reaction conditions described in the experimental methods in the ESI.† In summary, unless otherwise noted, a solar simulator provided illumination of 9 kW m^{-2} (9 suns, AM1.5) and no external heating was applied. The reactor was operated in flow mode with a gas flow of 8 ml min^{-1} : 8 ml min^{-1} : 4 ml min^{-1} H_2 : CO_2 : N_2 at 3.5 bar. No other products besides CH_4 and CO were detected, and no reactivity was observed for bare L and S supports upon illumination, while they solely produced CH_4 when externally heated to 180 °C without illumination. Confidence intervals of 98% are shown for catalyst activity. A summary of catalyst activity and selectivity is shown in Table S5.†

Accurate temperature measurements are essential for differentiating between thermal and non-thermal contributions. The catalyst temperature (Fig. 4c and S5a†) was measured with a thermocouple in the reactor vessel, a thermocouple at the bottom of the catalyst bed and fibre Bragg grating (FBG)-based fibre optic sensors inside the catalyst bed, as reported in a previous work (Fig. 4d and e).[26] A temperature difference of almost 100 °C is observed between the FBG result at the top of the catalyst surface compared to the thermocouple at the bottom of the catalyst bed. Furthermore, the presence of photothermal contributions in the reaction was investigated by studying the influence of light variation on the CO production, where the irradiance was varied between 6 kW m^{-2} and 9 kW m^{-2} (AM1.5) (6 and 9 suns). In order to eliminate the contribution of the semiconductor to the reaction, a UV cutoff filter (<395 nm) was mounted in the light path during additional experiments. All catalysts possess selectivity towards CO of more than 98%. An exponential relationship (Fig. 4a and b) is observed for 4Au/L-O, 4Au/S-O, 4Au/L-R and 4Au/S-R, confirming the presence of a photothermal contribution in all catalysts. As heat generated by plasmonic particles is linearly dependent on the incident light intensity, an

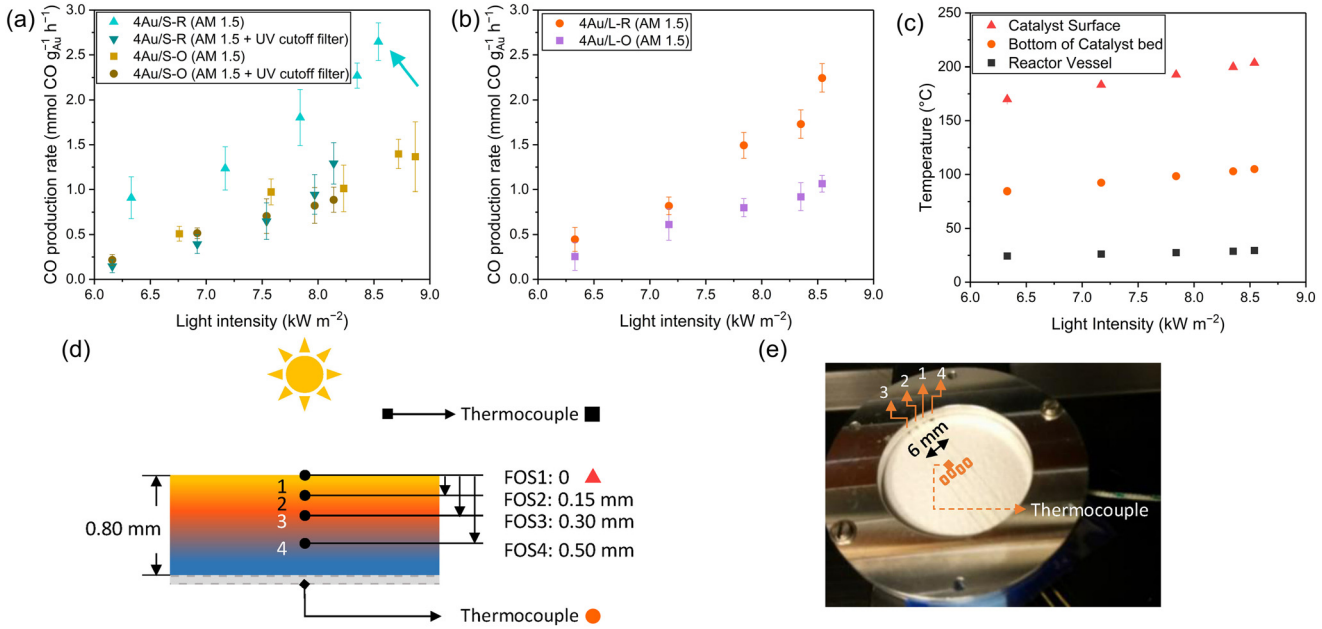

Fig. 4 (a) CO production of 4Au/S-R and 4Au/S-O under varied illumination using AM1.5 filter and AM1.5 + UV cutoff filter, (b) 4Au/L-R and 4Au/L-O under varied illumination using AM1.5 filter, (c) temperature of reactor vessel, bottom of the catalyst bed and top of the catalyst of 4Au/S-R irradiance variation experiments. Schematic (d) and photo (e) of the FBG-based fibre optic sensors inside the catalyst bed and thermocouples in the reactor; the figure has been adapted from a previously published work.[26] Reaction conditions: mixture of CO_2 : H_2 : N_2 (8 ml min^{-1} : 8 ml min^{-1} : 4 ml min^{-1}) at 3.5 bar pressure, 200 mg Au/CeO_{2-x} photocatalyst, varied irradiance from solar simulator (AM1.5 with and without UV cut-off filter).

exponential increase in activity is expected with light variation for photothermal processes, following Arrhenius' law.[35] No significant production (refer to Fig. S6a† for a simplified representation) difference can be observed between large (4Au/L-O and 4Au/L-R) and small (4Au/S-O and 4Au/S-R) CeO_{2-x} support samples, indicating that there is no direct significant impact of CeO_{2-x} surface area on the photocatalytic activity. From this it can be deduced that the pathway for the sunlight-driven rWGS reaction over Au/CeO_{2-x} is presumably not progressing through a redox mechanism, but instead through an associative mechanism, which aligns with reports in the literature.[52,101] Using the temperature at the catalyst surface from FBG, it was possible to calculate the apparent activation energy for the light-powered reaction using the Arrhenius equation (Fig. S7a–c†). Apparent activation energies of 1.2 kJ mol^{-1}, 1.0 kJ mol^{-1}, 1.2 kJ mol^{-1} and 0.8 kJ mol^{-1} were obtained for 4Au/L-O, 4Au/S-O, 4Au/L-R and 4Au/S-R, respectively. When making use of the UV cutoff filter, apparent activation energies of 1.0 kJ mol^{-1} and 1.7 kJ mol^{-1} were found for 4Au/S-O and 4Au/S-R, respectively. The apparent activation energy values obtained above are all very low compared to previously reported photocatalytic apparent activation energies of 146 kJ mol^{-1} for Au/CeO_2 (ref. 103) and 29 kJ mol^{-1} for Au/TiO_2 in the same reactor setup,[27] so an exceptionally active photocatalyst with very fast CO production would be expected. This, however, was not the case. A possible explanation could be that only a small fraction of the catalyst material is producing a significant amount of CO, while the majority of the catalyst material is not active, possibly amongst others due to limited light penetration into the catalyst bed (small skin depth). This can be demonstrated by examining the temperature depth profile within the catalyst bed during reaction (Fig. S5b†). The temperature of the 4Au/S-R photocatalyst upon 9 kW m^{-2} illumination is 203.3 °C at the surface, 197.8 °C at 0.15 mm depth, 193.3 °C at 0.30 mm depth and only 171.9 °C at 0.50 mm depth. Then, following Arrhenius' equation, about half CO production rate is expected at 0.30 mm depth and <10% CO production rate is expected at 0.50 mm depth. This was further confirmed by studying CO production (as a function of illuminated area) in relation to catalyst loading in the reactor (Fig. S8†). No homogeneous spread of catalyst over the holder could be achieved with catalyst loadings <50 mg, and from 60 mg catalyst loading onwards a plateau in CO production is reached. This confirms that the vast majority of photocatalytic activity takes place at the surface of the photocatalyst bed.

Another observation is a significant decrease in CO production for 4Au/S-R (Fig. 4a) when making use of the UV cutoff filter, paired with a significant increase in apparent activation energy, indicating a substantial contribution of CeO_{2-x} light absorption above bandgap. This difference in apparent activation energy could indicate a different rate-determining step in the catalytic cycle. This was not observed for 4Au/S-O under the same reaction conditions, where no impact of UV contribution was obtained. Wang *et al.*[101] recently reported that the plasmonic rWGS reaction over Au/Al_2O_3 is driven by an associative mechanism with both carboxylic and formate intermediates and V_Os acting as active sites. For smaller Au NPs (4.3 nm and 6.7 nm) the mechanism was found to be mainly dominated by mono- and bridged formate intermediates. The rate-determining

step was identified as the decomposition of HCOO* into CO* and OH* species, resulting in a cumulation of the formate intermediates on active sites during reaction. Applying this mechanism to our results, it can be interpreted that for 4Au/S-R the rate-determining step is similarly the dissociation of the formate intermediates, with an accumulation of these formate intermediates at the V_O sites. A reasonable explanation for the lower apparent activation energy upon UV illumination stems from additional charge carriers being generated in the semiconductor which aid in dissociation of the formate intermediate to form CO. In contrast, 4Au/S-O is in fact a precatalyst, as the active sites for catalysis, which are V_Os at the catalyst surface, still need to be generated, which lowers overall catalytic activity. No significant impact of UV irradiation is observed, indicating that UV-generated charge carriers generated in the CeO_{2-x} do not significantly contribute to the formation of oxygen vacancies compared to the LSPR effect.

Compared to Au/TiO_2 catalysts under similar reaction conditions and without external heating, our catalysts are outperformed in activity by Au/TiO_2 with small Au nanoparticles (1.6 nm).[25,27] The CO selectivity is similarly high (≥98%). For Au/TiO_2 catalysts with larger Au nanoparticles (6 nm, 16 nm) that activity is in the same range as for the Au/CeO_{2-x} catalysts reported in this manuscript.[30] Direct comparison with Au/Al_2O_3 and Au/SiO_2 is not possible, since the catalysts reported in the respective studies were both illuminated and externally heated to temperatures between 300 °C and 400 °C.[85,100–102] In a previous study on Au/CeO_2, Lu *et al.* reported a higher activity, albeit at a significantly higher irradiance of 32.0 kW m^{-2}.[103]

2.2.2 Dark reaction. When catalysis was performed without illumination, and using external thermal heating to 180 °C (Fig. 5), using L, 4Au/L-O, 4Au/L-R, S, 4Au/S-O and 4Au/S-R, a dramatic switch in selectivity of >97% towards CH_4 was observed for all samples. The highest catalyst activity was achieved with bare support L and S, indicating that a redox mechanism is likely at play in dark conditions. The lower CH_4 production upon deposition of Au, and higher activity of S compared to L, correlates well with the surface areas found in BET analysis of 4Au/L-O, 4Au/L-R, 4Au/S-O and 4Au/S-R compared to L and S, respectively. An explanation for this dramatic shift in selectivity at comparable reaction temperatures could be the absence of non-thermal contributions by the plasmonic particles upon illumination, generating charge carriers that allow for desorption of CO before further reduction to CH_4, as proposed in earlier work.[25,27,30,35,85]

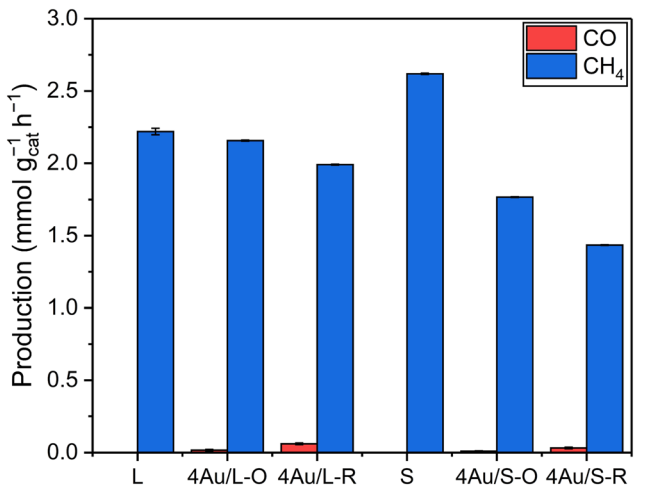

Fig. 5 CO and CH_4 production rates of L, 4Au/L-O, 4Au/L-R, S, 4Au/S-O and 4Au/S-R in the dark, thermally heated to 180 °C and no illumination. Reaction conditions: mixture of CO_2 : H_2 : N_2 (8 ml min^{-1} : 8 ml min^{-1} : 4 ml min^{-1}) at 3.5 bar pressure, 200 mg Au/CeO_{2-x} photocatalyst, no illumination and reactor heating to 180 °C.

2.2.3 The impact of Au particle size and loading. The catalytic activity (Fig. 6a) of the 0.4Au/S, 1.5Au/S and 6Au/S samples was investigated and CO production rates of 3.9 ± 0.7 mmol CO per g_{Au} per h, 1.0 ± 0.1 mmol CO per g_{Au} per h and 1.7 ± 0.2 mmol CO per g_{Au} per h were obtained, respectively. CH_4 production rates were 0.09 ± 0.02 mmol CH_4 per g_{Au} per h, 0.017 ± 0.002 mmol CH_4 per g_{Au} per h and 0.0054 ± 0.0005 mmol CH_4 per g_{Au} per h, respectively, resulting in a CO selectivity of 99.4%, 98.3% and 99.7% for 0.4Au/S, 1.5Au/S and 6Au/S. A higher CO production per gram of Au (g_{Au}^{-1}) for smaller Au particles is in line with the results of our previous study on TiO_2-supported Au.[30] However, our aim was to correlate the catalytic activity in the rWGS to physical properties of the catalyst. As noted above, V_O sites at the interface of the Au NP and the support are the likely active sites in the catalytic reaction. Therefore, the interface between Au NPs and the support was investigated and was quantified to be linearly dependent on the circumference of the base of a hemispherical Au NP on the support (in order to consider strong metal–support interaction). Based on this assumption, we calculated the circumference of the contact area of the Au hemisphere on CeO_{2-x} and multiplied this by the number of Au particles present in the catalyst (using Au loading by ICP and volume per hemisphere). For all three catalysts with different Au loading, we then divided the CO production rate by (number of Au particles × circumference). In addition, the relationship with the number of contact points, which scales with the number of Au particles in the catalyst, was investigated similarly assuming hemispherical Au particles.

The calculated values (Table S6†) represent catalytic activity normalised on the interface area between metal and support (scales linearly with the sum of circumferences of the base of all hemispherical Au NPs) (Fig. 6c) and normalised on the number of Au particles (Fig. 6b). The total volume of Au in the sample was considered. When normalising the CO production with respect to the weight of Au (Fig. 6a), significantly different values are obtained for the samples (0.4Au/S, 1.5Au/S and 6Au/S), which is also the case when normalising with respect to the number of Au particles.

This indicates that the Au weight or the number of Au particles are not directly determining the CO production rate. However, when the CO production rate is normalised on the

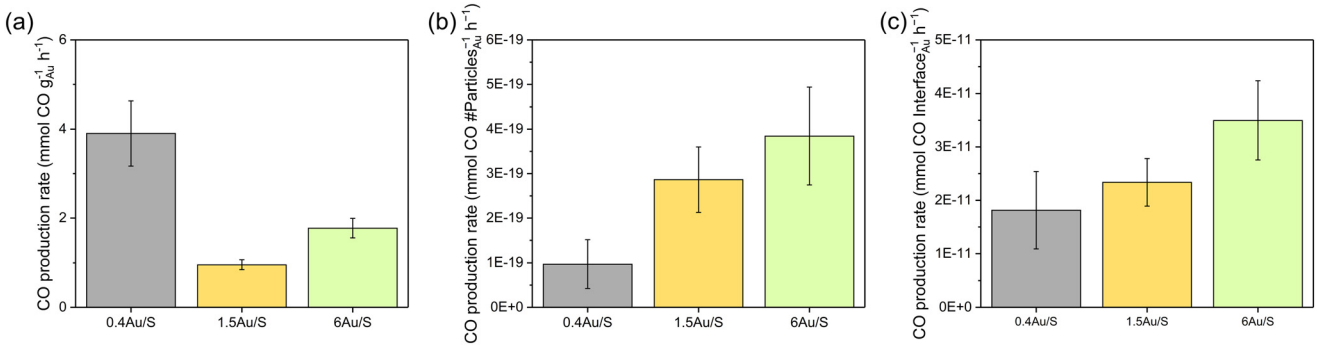

Fig. 6 CO production of 0.4Au/S, 1.5Au/S and 6.0 Au/S normalised on (a) mass of Au, (b) circumference of Au particles and (c) number of contact points (amount of Au particles). Reaction conditions: mixture of CO_2 : H_2 : N_2 (8 ml min^{-1} : 8 ml min^{-1} : 4 ml min^{-1}) at 3.5 bar pressure, 200 mg Au/CeO_{2-x} photocatalyst, 8.54 kW m^{-2} illumination from solar simulator (AM1.5).

interface area between metal and support, no significant differences were observed. This indicates that the CO production rate may scale directly with the number of active sites, which aligns with the associative mechanism reported above. As such, the CO production rate is expected to increase linearly with the number of active sites as it will increase the dissociation of formate intermediates. As a verification, the same calculations were performed for 4Au/L-O, 4 Au/L-R, 4Au/S-O and 4Au/S-R (Fig. S6b†) and similarly no significant differences between samples could be observed, indicating that the difference in CO activity between reduced and oxidised samples could be attributed to Au particle growth in oxidised samples. These observations underline careful consideration when choosing a plasmonic metal deposition method on semiconducting supports for the sunlight-driven rWGS, as the activity of the photocatalyst is strongly dependent on the interfacial sites.

2.2.4 Catalyst stability. Spent catalysts of Au/L-O, Au/S-O, Au/L-R and Au/S-R were characterised after catalysis with HAADF-STEM (Fig. S9a, c, d and f†) and no significant differences were observed compared to the as-synthesised catalysts. Diffuse reflectance UV-vis spectroscopy (Fig. S9b†) shows no difference in the Au LSPR absorption band for 4Au/L-R and 4Au/S-R. However, for 4Au/L-O and 4Au/S-O the redshifted shoulder discussed for the fresh catalysts, which was attributed to formation of Au dimers during particle growth during the thermal treatment, reduces in intensity. This could be an indication that the temperature in the plasmonic dimer NPs during catalysis is adequate to coalesce these Au dimers into spherical particles, which are only slightly redshifted compared to the smaller Au NPs. However, not enough energy is present for Au particles to migrate over the surface, so no additional particle growth takes place. Raman spectra (Fig. S2c†) did not yield significantly different results compared to the as-synthesised catalysts. We studied the difference in the amount of oxygen vacancies in oxidized and reduced catalysts under catalytic conditions. Comparing H_2-TPR results obtained for reduced catalysts 4Au/L-R and 4Au/S-R before and after catalysis demonstrates that the percentage of H_2 uptake increases after catalysis, indicating a partial loss of oxygen vacancies. Before catalysis, the percentage of H_2 uptake was 16.0% and 20.6% for 4Au/L-R and 4Au/S-R, respectively (Fig. S9e and Table S4†). After catalysis, this increased to 18.2% and 22.5%. For the oxidized catalysts 4Au/L-O and 4Au/S-O, the percentage dropped during catalysis from 25.7% to 16.7% and from 30.6% to 24.3%, respectively. Therefore, the applied reaction conditions during catalysis influence V_Os.

The stability of CO production of the 4Au/S-R catalyst was investigated over 38 h (Fig. 7a). Initially a CO production rate of 2.42 ± 0.06 mmol CO per g_{Au} per h was obtained, and after 38 h 1.59 ± 0.05 mmol CO per g_{Au} per h was observed, resulting in an activity loss of 34%. This loss in activity could be fully attributed to H_2O accumulation on the surface at V_O sites, effectively poisoning the active sites for rWGS. The reactor was left at 90 °C under vacuum for 2 h and then allowed to cool, allowing the catalyst to fully regenerate. A CO production rate of 2.53 ± 0.09 mmol CO per g_{Au} per h was found upon illumination. Similar results were found for 4Au/S-O over 15 h (Fig. S10†), with an initial CO production rate of 1.87 ± 0.06 mmol CO per g_{Au} per h and a CO production rate of 0.84 ± 0.06 mmol CO per g_{Au} per h after 15 h with an activity loss of 55%. The catalyst could similarly be regenerated under vacuum at 90 °C for 2 h and a CO production rate of 1.7 ± 0.1 mmol CO per g_{Au} per h upon illumination. On–off experiments were carried out to probe catalyst stability with a fluctuating irradiance (Fig. 7b). The lamp was turned on for 1 h and then turned off for 1 h per cycle. 4 of these cycles were performed during one day. The catalyst remained under dark conditions at room temperature overnight. The following day, 4 more cycles were performed. Similar losses of CO production due to accumulation of H_2O at the catalyst surface were observed. In practical application, the catalyst may be regenerated, *e.g.* by thermal treatment or *in vacuo*. Furthermore, for equilibrium-limited reactions such as the rWGS process, adsorption of water as a reaction product increases the conversion by shifting the equilibrium according to Le Chatelier's principle. Sorbents and/or membrane technology are applied to achieve this and facilitate CO_2 capture and utilization.[108]

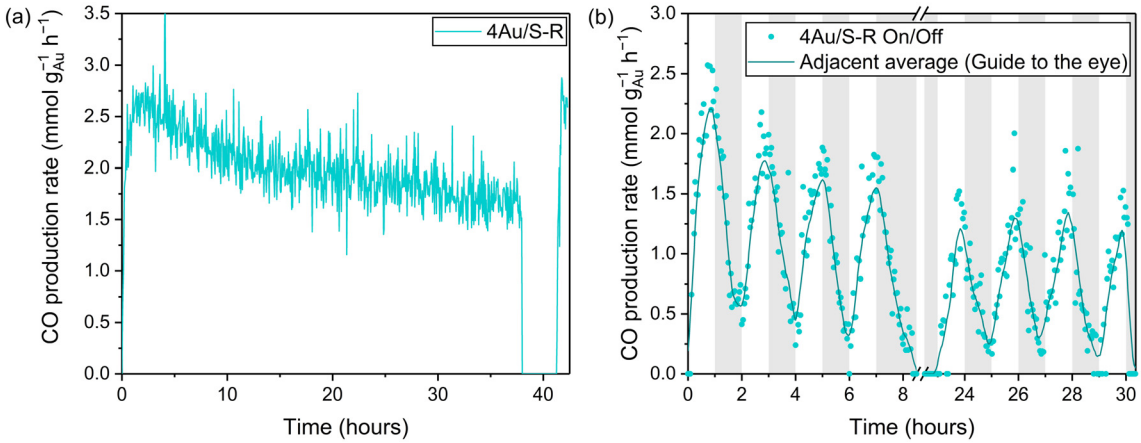

Fig. 7 (a) CO production of 4Au/S-R over 38 h, CO production after regeneration in vacuum at 90 °C has been appended at 40 h, and (b) CO production of 4Au/S-R during on–off experiments, the lamp was turned on–off every hour. Reaction conditions: mixture of CO_2 : H_2 : N_2 (8 ml min^{-1} : 8 ml min^{-1} : 4 ml min^{-1}) at 3.5 bar pressure, 200 mg Au/CeO_{2-x} photocatalyst, 8.54 kW m^{-2} illumination from solar simulator (AM1.5).

2.2.5 Reaction mechanism. The results obtained from the catalysis study clearly demonstrate that the role of plasmonic Au in the Au/CeO_{2-x}-catalyzed rWGS reaction is essential. It contributes in two ways: (i) plasmon-induced charge carriers induce rapid desorption of CO from the catalyst surface, avoiding further reduction to CH_4, and (ii) electron–phonon coupling leads to an increase in temperature thereby increasing the reaction rate. Furthermore, the influence of UV irradiation on the reaction rate obtained with reduced Au/CeO_{2-x} catalysts and the linear dependence of the reaction rate on the interface area between metal and support suggest that catalysis takes place at the interface of Au and CeO_{2-x}, pointing out to an associative mechanism for the plasmon-catalyzed rWGS reaction. A proposed reaction mechanism, mediated by monobridged formate, is shown in Fig. 8, following the proposed mechanism of plasmonic-driven rWGS over Au/Al_2O_3 as recently reported by Wang *et al.*[101] The activation energy of the Au/CeO_{2-x}-catalyzed rWGS reaction is very low (1–2 kJ mol^{-1}), which is paradoxical given the low CO production rate. This may be explained by the limited number of active sites on the catalyst combined with the very limited light penetration depth. Future work should focus on detailed investigation of the active sites. An in-depth study of the dependence of the reaction rate and activation energy on the size of the Au particles, whilst keeping the light penetration depth constant by tailoring the Au loading, may further contribute to identifying the catalytically active site. In analogy to the recent work by Duan and coworkers, these kinetic data, together with mesokinetic modeling, may provide a quantitative description of active site characteristics.[109,110]

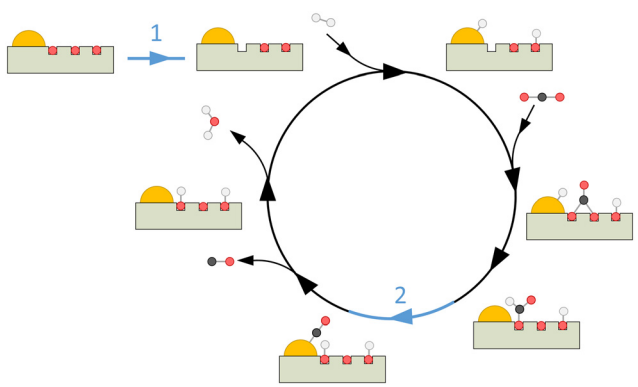

Fig. 8 Proposed associative monobridged formate-mediated reaction mechanism for the plasmonic-driven rWGS reaction over Au/CeO_{2-x} upon illumination. In fully oxidised catalysts, the rate-determining step (blue 1) is the plasmonic-driven generation of vacancies near Au NPs. For catalysts with a reducing treatment, the rate-determining step (blue 2) is proposed to be the dissociation of the formate intermediate. Atoms are labelled as Au (gold), C (black), H (white), O (red).

3 Conclusion

We successfully produced CeO_{2-x} support materials by hydrothermal synthesis and decorated them with Au nanoparticles on their surface. For systematic catalytic studies, we produced materials with varying CeO_{2-x} particle size, Au particle size and loading, and concentration of oxygen vacancies. In addition to conventional compositional and structural characterization, we determined the H_2 uptake of these materials as a function of temperature to shed light on the concentration of oxygen vacancies before and after catalysis. We determined that both photothermal and non-thermal effects contributed to the light-driven rWGS reaction catalysed by plasmonic Au/CeO_{2-x}. Upon illumination, all Au/CeO_{2-x} catalysts tested in this study produced CO with a selectivity of ≥98% at low catalyst surface temperatures (up to 203 °C). The supports without Au were inactive. The exponential relationship between the CO production rate and the irradiance confirms the contribution of photothermal heating. For all tested catalysts, low apparent activation energies were obtained (0.8–1.7 kJ mol^{-1}). The contrasting

low overall activity of the tested catalysts (up to 2.6 ± 0.2 mmol g^{-1} h^{-1}) is amongst others due to the limited light penetration depth. UV light only contributed to the performance of reduced catalysts. Their oxidized counterparts remained unaffected. The latter is likely due to the fact that oxidized Au/CeO_2 is merely a precatalyst, for which the formation of oxygen vacancies to form the actual catalyst is rate determining. For the reduced catalysts, we assume that the decomposition of formate intermediates is rate determining (associative mechanism). In the dark, all Au/CeO_{2-x} catalysts and the supports without Au formed CH_4 instead of CO. The latter indicates that plasmon-induced desorption of CO plays a vital role in preventing further reduction to CH_4. Systematic studies with varying Au loading and particle size show a linear dependence of the catalytic activity on the accessible interfacial area between CeO_{2-x} and Au. This observation is in line with the proposed associative mechanism for which the rate-determining decomposition of formate takes place at the metal–support interface. An assessment of the catalyst stability in steady-state and fluctuating operating conditions demonstrated that the catalytic performance was affected by adsorption of H_2O as reaction product, which could be reversed upon heating *in vacuo*. For spent catalysts, we observed that the concentration of oxygen vacancies substantially increased for oxidized Au/CeO_2, whilst it remained similar for their reduced counterparts. This confirms the formation of active catalyst by reduction of the oxidized precatalyst. Structural changes were not observed for spent catalysts, indicating good stability under the applied reaction conditions.

Data availability

All data are available in the manuscript and the submitted ESI† file. For raw data, please contact the corresponding authors.

Author contributions

Jordi Volders: conceptualisation, data curation, formal analysis, investigation, methodology, visualisation, writing – original draft, writing – review & editing. Sander Bossier: investigation, writing – review & editing. Sander Stulens: investigation, visualisation, writing – review & editing. Bjorn Joos: investigation, writing – review & editing. Thomas Vranken: methodology, resources, writing – review & editing. Francesc Sastre: formal analysis, investigation, methodology, resources, writing – review & editing. Jan D'Haen: investigation, visualisation, writing – review & editing. Ken Elen: conceptualisation, data curation, funding acquisition, methodology, supervision, writing – review & editing. Marcel A. Verheijen: funding acquisition, investigation, methodology, resources, visualisation, writing – review & editing. Pegie Cool: funding acquisition, methodology, supervision, writing – review & editing. An Hardy: conceptualisation, data curation, funding acquisition, methodology, supervision, writing – review & editing. Pascal Buskens: conceptualisation, data curation, funding acquisition, methodology, supervision, writing – review & editing. Marlies K. Van Bael: conceptualisation, data curation, funding acquisition, methodology, supervision, writing – review & editing. All authors have read and agreed to the published version of the manuscript.

Conflicts of interest

There are no conflicts to declare.

Acknowledgements

This work received funding from the European Union's Horizon 2020 research and innovation programme under grant agreement 101015960 (SPOTLIGHT), the EC Interreg Flanders-The Netherlands project FOTON and the Research Foundation Flanders (FWO-Vlaanderen) under project No. G0A4924N (PICaSSo). Solliance and the Dutch province of Noord-Brabant are acknowledged for funding the TEM facility. We would like to thank Robbe Jacops for ICP-OES measurements, Pieter De Meyer for TGA analyses and Naomi Billiet and Nele Debusschere for XRD measurements.

References

1 IEA, Key World Energy Statistics 2021, **https://www.iea.org/reports/key-world-energy-statistics-2021**, (accessed 25/06/2024).
2 J. Artz, T. E. Müller, K. Thenert, J. Kleinekorte, R. Meys, A. Sternberg, A. Bardow and W. Leitner, Sustainable Conversion of Carbon Dioxide: An Integrated Review of Catalysis and Life Cycle Assessment, *Chem. Rev.*, 2018, **118**, 434–504.
3 J. H. Clark, T. J. Farmer, L. Herrero-Davila and J. Sherwood, Circular economy design considerations for research and process development in the chemical sciences, *Green Chem.*, 2016, **18**, 3914–3934.
4 L. Guo, J. Sun, Q. Ge and N. Tsubaki, Recent advances in direct catalytic hydrogenation of carbon dioxide to valuable C2+ hydrocarbons, *J. Mater. Chem. A*, 2018, **6**, 23244–23262.
5 A. Rafiee, K. Rajab Khalilpour, D. Milani and M. Panahi, Trends in CO_2 conversion and utilization: A review from process systems perspective, *J. Environ. Chem. Eng.*, 2018, **6**, 5771–5794.
6 A. I. Osman, M. Hefny, M. I. A. Abdel Maksoud, A. M. Elgarahy and D. W. Rooney, Recent advances in carbon capture storage and utilisation technologies: a review, *Environ. Chem. Lett.*, 2021, **19**, 797–849.
7 F. Sastre, A. V. Puga, L. Liu, A. Corma and H. García, Complete Photocatalytic Reduction of CO_2 to Methane by H_2 under Solar Light Irradiation, *J. Am. Chem. Soc.*, 2014, **136**, 6798–6801.
8 F. Sastre, A. Corma and H. García, Visible-Light Photocatalytic Conversion of Carbon Monoxide to Methane by Nickel(II) Oxide, *Angew. Chem., Int. Ed.*, 2013, **52**, 12983–12987.

9 R. Franke, D. Selent and A. Börner, Applied Hydroformylation, *Chem. Rev.*, 2012, **112**, 5675–5732.
10 W. Gao, R. Gao, Y. Zhao, M. Peng, C. Song, M. Li, S. Li, J. Liu, W. Li, Y. Deng, M. Zhang, J. Xie, G. Hu, Z. Zhang, R. Long, X.-D. Wen and D. Ma, Photo-Driven Syngas Conversion to Lower Olefins over Oxygen-Decorated Fe_5C_2 Catalyst, *Chem*, 2018, **4**, 2917–2928.
11 G. J. Sunley and D. J. Watson, High productivity methanol carbonylation catalysis using iridium: The Cativa™ process for the manufacture of acetic acid, *Catal. Today*, 2000, **58**, 293–307.
12 J. R. Rostrup-Nielsen, New aspects of syngas production and use, *Catal. Today*, 2000, **63**, 159–164.
13 P. Kaiser, R. B. Unde, C. Kern and A. Jess, Production of Liquid Hydrocarbons with CO_2 as Carbon Source based on Reverse Water-Gas Shift and Fischer-Tropsch Synthesis, *Chem. Ing. Tech.*, 2013, **85**, 489–499.
14 R. Detz, M. Beerse, N. Meulendijks, P. Buskens and B. van der Zwaan, Towards the Use of Renewable Syngas for the Decarbonization of Industry, *ChemSusChem*, 2024, e202400059.
15 C. Xavier Silva, J. Moncada Botero, F. Sastre, J. van den Ham, P. Buskens, N. Meulendijks and R. J. Detz, Techno-economic analysis for the sunlight-powered reverse water gas shift process: Scenarios, costs, and comparative insights, *Sustain. Energy Technol. Assessments*, 2024, **65**, 103768.
16 P. Frontera, A. Macario, M. Ferraro and P. Antonucci, Supported Catalysts for CO_2 Methanation: A Review, *Catalysts*, 2017, **7**, 59.
17 X. Su, X. Yang, B. Zhao and Y. Huang, Designing of highly selective and high-temperature endurable RWGS heterogeneous catalysts: recent advances and the future directions, *J. Energy Chem.*, 2017, **26**, 854–867.
18 Y. A. Daza and J. N. Kuhn, CO_2 conversion by reverse water gas shift catalysis: comparison of catalysts, mechanisms and their consequences for CO_2 conversion to liquid fuels, *RSC Adv.*, 2016, **6**, 49675–49691.
19 X. Li, J. Yu, M. Jaroniec and X. Chen, Cocatalysts for Selective Photoreduction of CO_2 into Solar Fuels, *Chem. Rev.*, 2019, **119**, 3962–4179.
20 J. Low, J. Yu, M. Jaroniec, S. Wageh and A. A. Al-Ghamdi, Heterojunction Photocatalysts, *Adv. Mater.*, 2017, **29**, 1601694.
21 M. D. Khan, I. Fareed, M. ul Hassan Farooq, M. Akram, S. ur Rehman, Z. Ali, Z. Tariq, M. Irshad, C. Li and F. K. Butt, Methodologies for enriched photocatalytic CO_2 reduction: an overview, *Int. J. Environ. Sci. Technol.*, 2024, **21**, 3489–3526.
22 D. Burova, J. Rohlfs, F. Sastre, P. M. Molina, N. Meulendijks, M. A. Verheijen, A.-S. Kelchtermans, K. Elen, A. Hardy, M. K. Van Bael and P. Buskens, Comparing the Performance of Supported Ru Nanocatalysts Prepared by Chemical Reduction of $RuCl_3$ and Thermal Decomposition of $Ru_3(CO)_{12}$ in the Sunlight-Powered Sabatier Reaction, *Catalysts*, 2022, **12**, 284.
23 R. Grote, R. Habets, J. Rohlfs, F. Sastre, N. Meulendijks, M. Xu, M. A. Verheijen, K. Elen, A. Hardy, M. K. Van Bael, T. den Hartog and P. Buskens, Collective photothermal effect of Al_2O_3-supported spheroidal plasmonic Ru nanoparticle catalysts in the sunlight-powered Sabatier reaction, *ChemCatChem*, 2020, **12**, 5618–5622.
24 J. Rohlfs, K. W. Bossers, N. Meulendijks, F. Valega Mackenzie, M. Xu, M. A. Verheijen, P. Buskens and F. Sastre, Continuous-Flow Sunlight-Powered CO_2 Methanation Catalyzed by γ-Al_2O_3-Supported Plasmonic Ru Nanorods, *Catalysts*, 2022, **12**, 126.
25 P. Martínez Molina, K. W. Bossers, J. D. Wienk, J. Rohlfs, N. Meulendijks, M. A. Verheijen, P. Buskens and F. Sastre, Sunlight Powered Continuous Flow Reverse Water Gas Shift Process Using a Plasmonic Au/TiO_2 Nanocatalyst, *Chem. – Asian J.*, 2023, **18**, e202300405.
26 M. Xu, T. den Hartog, L. Cheng, M. Wolfs, R. Habets, J. Rohlfs, J. van den Ham, N. Meulendijks, F. Sastre and P. Buskens, Using Fiber Bragg Grating Sensors to Quantify Temperature Non-Uniformities in Plasmonic Catalyst Beds under Illumination, *ChemPhotoChem*, 2022, **6**, e202100289.
27 P. Martínez Molina, N. Meulendijks, M. Xu, M. A. Verheijen, T. den Hartog, P. Buskens and F. Sastre, Low Temperature Sunlight-Powered Reduction of CO_2 to CO Using a Plasmonic Au/TiO_2 Nanocatalyst, *ChemCatChem*, 2021, **13**, 4507–4513.
28 J. H. A. Schuurmans, T. M. Masson, S. D. A. Zondag, P. Buskens and T. Noël, Solar-Driven Continuous CO_2 Reduction to CO and CH_4 using Heterogeneous Photothermal Catalysts: Recent Progress and Remaining Challenges, *ChemSusChem*, 2024, **17**, e202301405.
29 F. Sastre, C. Versluis, N. Meulendijks, J. Rodríguez-Fernández, J. Sweelssen, K. Elen, M. K. Van Bael, T. den Hartog, M. A. Verheijen and P. Buskens, Sunlight-Fueled, Low-Temperature Ru-Catalyzed Conversion of CO_2 and H_2 to CH_4 with a High Photon-to-Methane Efficiency, *ACS Omega*, 2019, **4**, 7369–7377.
30 J. Volders, K. Elen, A. Raes, R. Ninakanti, A.-S. Kelchtermans, F. Sastre, A. Hardy, P. Cool, S. W. Verbruggen, P. Buskens and M. K. Van Bael, Sunlight-Powered Reverse Water Gas Shift Reaction Catalysed by Plasmonic Au/TiO_2 Nanocatalysts: Effects of Au Particle Size on the Activity and Selectivity, *Nanomaterials*, 2022, **12**, 4153.
31 A. Moores and F. Goettmann, The plasmon band in noble metal nanoparticles: an introduction to theory and applications, *New J. Chem.*, 2006, **30**, 1121–1132.
32 A. Gellé and A. Moores, Plasmonic nanoparticles: Photocatalysts with a bright future, *Curr. Opin. Green Sustainable Chem.*, 2019, **15**, 60–66.
33 R.-G. Ciocarlan, N. Blommaerts, S. Lenaerts, P. Cool and S. W. Verbruggen, Recent Trends in Plasmon-Assisted Photocatalytic CO_2 Reduction, *ChemSusChem*, 2023, **16**, e202201647.
34 G. Baffou and R. Quidant, Nanoplasmonics for chemistry, *Chem. Soc. Rev.*, 2014, **43**, 3898–3907.
35 G. Baffou, I. Bordacchini, A. Baldi and R. Quidant, Simple experimental procedures to distinguish photothermal from hot-carrier processes in plasmonics, *Light: Sci. Appl.*, 2020, **9**, 108.

36 R. Asapu, N. Claes, R.-G. Ciocarlan, M. Minjauw, C. Detavernier, P. Cool, S. Bals and S. W. Verbruggen, Electron Transfer and Near-Field Mechanisms in Plasmonic Gold-Nanoparticle-Modified TiO_2 Photocatalytic Systems, *ACS Appl. Nano Mater.*, 2019, **2**, 4067–4074.

37 G. Baffou, F. Cichos and R. Quidant, Applications and challenges of thermoplasmonics, *Nat. Mater.*, 2020, **19**, 946–958.

38 Y. Sivan, J. H. Baraban and Y. Dubi, Experimental practices required to isolate thermal effects in plasmonic photocatalysis: lessons from recent experiments, *OSA Continuum*, 2020, **3**, 483–497.

39 Y. Dubi and Y. Sivan, "Hot" electrons in metallic nanostructures—non-thermal carriers or heating?, *Light: Sci. Appl.*, 2019, **8**, 89.

40 Y. Dubi, I. W. Un and Y. Sivan, Thermal effects – an alternative mechanism for plasmon-assisted photocatalysis, *Chem. Sci.*, 2020, **11**, 5017–5027.

41 R. Kamarudheen, G. J. W. Aalbers, R. F. Hamans, L. P. J. Kamp and A. Baldi, Distinguishing Among All Possible Activation Mechanisms of a Plasmon-Driven Chemical Reaction, *ACS Energy Lett.*, 2020, **5**, 2605–2613.

42 A. Trovarelli, Catalytic Properties of Ceria and CeO_2-Containing Materials, *Catal. Rev.: Sci. Eng.*, 1996, **38**, 439–520.

43 A. Trovarelli, C. de Leitenburg and G. Dolcetti, CO and CO_2 hydrogenation under transient conditions over Rh–CeO_2: novel positive effects of metal–support interaction on catalytic activity and selectivity, *J. Chem. Soc., Chem. Commun.*, 1991, 472–473, DOI: **10.1039/C39910000472**.

44 P. Ebrahimi, A. Kumar and M. Khraisheh, A Review of CeO_2 Supported Catalysts for CO_2 Reduction to CO through the Reverse Water Gas Shift Reaction, *Catalysts*, 2022, **12**, 1101.

45 M. Boaro, S. Colussi and A. Trovarelli, Ceria-Based Materials in Hydrogenation and Reforming Reactions for CO_2 Valorization, *Front. Chem.*, 2019, **7**, 28, DOI: **10.3389/fchem.2019.00028**.

46 A. E. Herzog, T. J. Michael, A. D. Dunkelberger, M. D. Johannes, D. R. Rolison, P. A. DeSario and T. G. Novak, Nanostructured CeO_2 photocatalysts: optimizing surface chemistry, morphology, and visible-light absorption, *Nanoscale*, 2024, **16**, 9659–9679, DOI: **10.1039/D4NR00676C**.

47 T. Montini, M. Melchionna, M. Monai and P. Fornasiero, Fundamentals and Catalytic Applications of CeO_2-Based Materials, *Chem. Rev.*, 2016, **116**, 5987–6041.

48 M. Melchionna and P. Fornasiero, The role of ceria-based nanostructured materials in energy applications, *Mater. Today*, 2014, **17**, 349–357.

49 A. Goguet, F. C. Meunier, D. Tibiletti, J. P. Breen and R. Burch, Spectrokinetic Investigation of Reverse Water-Gas-Shift Reaction Intermediates over a Pt/CeO_2 Catalyst, *J. Phys. Chem. B*, 2004, **108**, 20240–20246.

50 L. Lin, S. Yao, Z. Liu, F. Zhang, N. Li, D. Vovchok, A. Martínez-Arias, R. Castañeda, J. Lin, S. D. Senanayake, D. Su, D. Ma and J. A. Rodriguez, In Situ Characterization of Cu/CeO_2 Nanocatalysts for CO_2 Hydrogenation: Morphological Effects of Nanostructured Ceria on the Catalytic Activity, *J. Phys. Chem. C*, 2018, **122**, 12934–12943.

51 M. Li, T. H. My Pham, Y. Ko, K. Zhao, L. Zhong, W. Luo and A. Züttel, Support-Dependent Cu–In Bimetallic Catalysts for Tailoring the Activity of Reverse Water Gas Shift Reaction, *ACS Sustainable Chem. Eng.*, 2022, **10**, 1524–1535.

52 M. Ziemba, J. Weyel and C. Hess, Elucidating the mechanism of the reverse water–gas shift reaction over Au/CeO_2 catalysts using operando and transient spectroscopies, *Appl. Catal., B*, 2022, **301**, 120825.

53 M. Zhu, Q. Ge and X. Zhu, Catalytic Reduction of CO_2 to CO via Reverse Water Gas Shift Reaction: Recent Advances in the Design of Active and Selective Supported Metal Catalysts, *Trans. Tianjin Univ.*, 2020, **26**, 172–187.

54 E. Pahija, C. Panaritis, S. Gusarov, J. Shadbahr, F. Bensebaa, G. Patience and D. C. Boffito, Experimental and Computational Synergistic Design of Cu and Fe Catalysts for the Reverse Water–Gas Shift: A Review, *ACS Catal.*, 2022, **12**, 6887–6905.

55 L. F. Bobadilla, J. L. Santos, S. Ivanova, J. A. Odriozola and A. Urakawa, Unravelling the Role of Oxygen Vacancies in the Mechanism of the Reverse Water–Gas Shift Reaction by Operando DRIFTS and Ultraviolet–Visible Spectroscopy, *ACS Catal.*, 2018, **8**, 7455–7467.

56 H. Dong, M. Jung, Y. Zhang, S. Wang and S. Ding, Supported noble metal-based catalysts for thermal CO_2 hydrogenation to CO, *Mol. Catal.*, 2024, **560**, 114133.

57 A. Vourros, I. Garagounis, V. Kyriakou, S. A. C. Carabineiro, F. J. Maldonado-Hódar, G. E. Marnellos and M. Konsolakis, Carbon dioxide hydrogenation over supported Au nanoparticles: Effect of the support, *J. CO2 Util.*, 2017, **19**, 247–256.

58 S.-Y. Lai, Y. Qiu and S. Wang, Effects of the structure of ceria on the activity of gold/ceria catalysts for the oxidation of carbon monoxide and benzene, *J. Catal.*, 2006, **237**, 303–313.

59 Q. Fu, S. Kudriavtseva, H. Saltsburg and M. Flytzani-Stephanopoulos, Gold–ceria catalysts for low-temperature water-gas shift reaction, *Chem. Eng. J.*, 2003, **93**, 41–53.

60 U. R. Pillai and S. Deevi, Highly active gold-ceria catalyst for the room temperature oxidation of carbon monoxide, *Appl. Catal., A*, 2006, **299**, 266–273.

61 S. A. C. Carabineiro, S. S. T. Bastos, J. J. M. Órfão, M. F. R. Pereira, J. J. Delgado and J. L. Figueiredo, Exotemplated ceria catalysts with gold for CO oxidation, *Appl. Catal., A*, 2010, **381**, 150–160.

62 L. G. A. van de Water, S. K. Wilkinson, R. A. P. Smith and M. J. Watson, Understanding methanol synthesis from CO/H_2 feeds over Cu/CeO_2 catalysts, *J. Catal.*, 2018, **364**, 57–68.

63 X. Zhu, X. Qu, X. Li, J. Liu, J. Liu, B. Zhu and C. Shi, Selective reduction of carbon dioxide to carbon monoxide over Au/CeO_2 catalyst and identification of reaction intermediate, *Chin. J. Catal.*, 2016, **37**, 2053–2058.

64 S. Li, Y. Xu, Y. Chen, W. Li, L. Lin, M. Li, Y. Deng, X. Wang, B. Ge, C. Yang, S. Yao, J. Xie, Y. Li, X. Liu and D. Ma, Tuning the Selectivity of Catalytic Carbon Dioxide Hydrogenation over Iridium/Cerium Oxide Catalysts with a

Strong Metal–Support Interaction, *Angew. Chem., Int. Ed.*, 2017, **56**, 10761–10765.

65 G. Kim, S. Shin, Y. Choi, J. Kim, G. Kim, K.-J. Kim and H. Lee, Gas-Permeable Iron-Doped Ceria Shell on Rh Nanoparticles with High Activity and Durability, *JACS Au*, 2022, **2**, 1115–1122.

66 S. Li, Y. Xu, H. Wang, B. Teng, Q. Liu, Q. Li, L. Xu, X. Liu and J. Lu, Tuning the CO_2 Hydrogenation Selectivity of Rhodium Single-Atom Catalysts on Zirconium Dioxide with Alkali Ions, *Angew. Chem., Int. Ed.*, 2023, **62**, e202218167.

67 S. Mine, T. Yamaguchi, K. W. Ting, Z. Maeno, S. M. A. H. Siddiki, K. Oshima, S. Satokawa, K.-i. Shimizu and T. Toyao, Reverse water-gas shift reaction over $Pt/MoO_x/TiO_2$: reverse Mars–van Krevelen mechanism via redox of supported MoO_x, *Catal. Sci. Technol.*, 2021, **11**, 4172–4180.

68 A. S. Malik, H. Bali, F. Czirok, Á. Szamosvölgyi, G. Halasi, A. Efremova, B. Šmíd, A. Sápi, Á. Kukovecz and Z. Kónya, Turning CO_2 to CH_4 and CO over CeO_2 and MCF-17 supported Pt, Ru and Rh nanoclusters – Influence of nanostructure morphology, supporting materials and operating conditions, *Fuel*, 2022, **326**, 124994.

69 L. C. Wang, D. Widmann and R. J. Behm, Reactive removal of surface oxygen by H_2, CO and CO/H_2 on a Au/CeO_2 catalyst and its relevance to the preferential CO oxidation (PROX) and reverse water gas shift (RWGS) reaction, *Catal. Sci. Technol.*, 2015, **5**, 925–941.

70 L. C. Wang, M. Tahvildar Khazaneh, D. Widmann and R. J. Behm, TAP reactor studies of the oxidizing capability of CO_2 on a Au/CeO_2 catalyst – A first step toward identifying a redox mechanism in the Reverse Water–Gas Shift reaction, *J. Catal.*, 2013, **302**, 20–30.

71 Y. Guo and H. Thérien-Aubin, Nanofibrous Photocatalytic Membranes Based on Tailored Anisotropic Gold/Ceria Nanoparticles, *ACS Appl. Mater. Interfaces*, 2021, **13**, 37578–37588.

72 B. Li, B. Zhang, S. Nie, L. Shao and L. Hu, Optimization of plasmon-induced photocatalysis in electrospun Au/CeO_2 hybrid nanofibers for selective oxidation of benzyl alcohol, *J. Catal.*, 2017, **348**, 256–264.

73 E. I. García-López, Z. Abbasi, F. Parrino, V. La Parola, L. F. Liotta and G. Marcì, Au/CeO_2 Photocatalyst for the Selective Oxidation of Aromatic Alcohols in Water under UV, Visible and Solar Irradiation, *Catalysts*, 2021, **11**, 1467.

74 W. Zhao, Q. Dong, C. Sun, D. Xia, H. Huang, G. Yang, G. Wang and D. Y. C. Leung, A novel $Au/g\text{-}C_3N_4$ nanosheets/CeO_2 hollow nanospheres plasmonic heterojunction photocatalysts for the photocatalytic reduction of hexavalentchromium and oxidation of oxytetracycline hydrochloride, *Chem. Eng. J.*, 2021, **409**, 128185.

75 A. Taratayko, Y. Larichev, V. Zaikovskii, N. Mikheeva and G. Mamontov, $Ag–CeO_2$/SBA-15 composite prepared from Pluronic P123@SBA-15 hybrid as catalyst for room-temperature reduction of 4-nitrophenol, *Catal. Today*, 2021, **375**, 576–584.

76 D. V. Dao, T. T. D. Nguyen, P. Uthirakumar, Y.-H. Cho, G.-C. Kim, J.-K. Yang, D.-T. Tran, T. D. Le, H. Choi, H. Y. Kim, Y.-T. Yu and I.-H. Lee, Insightful understanding of hot-carrier generation and transfer in plasmonic $Au@CeO_2$ core–shell photocatalysts for light-driven hydrogen evolution improvement, *Appl. Catal., B*, 2021, **286**, 119947.

77 J.-H. Wang, M. Chen, Z.-J. Luo, L. Ma, Y.-F. Zhang, K. Chen, L. Zhou and Q.-Q. Wang, Ceria-Coated Gold Nanorods for Plasmon-Enhanced Near-Infrared Photocatalytic and Photoelectrochemical Performances, *J. Phys. Chem. C*, 2016, **120**, 14805–14812.

78 A. A. Fauzi, A. A. Jalil, N. S. Hassan, F. F. A. Aziz, M. S. Azami, I. Hussain, R. Saravanan and D. V. N. Vo, A critical review on relationship of CeO_2-based photocatalyst towards mechanistic degradation of organic pollutant, *Chemosphere*, 2022, **286**, 131651.

79 S. Ali, S. Basak, S. Sikdar and M. Roy, Synergetic effects of green synthesized CeO_2 nanorod-like catalyst for degradation of organic pollutants to reduce water pollution, *Environ. Nanotechnol., Monit. Manage.*, 2021, **16**, 100539.

80 J. Shen, J. Shen, W. Zhang, X. Yu, H. Tang, M. Zhang, Zulfiqar and Q. Liu, Built-in electric field induced CeO_2/Ti_3C_2-MXene Schottky-junction for coupled photocatalytic tetracycline degradation and CO_2 reduction, *Ceram. Int.*, 2019, **45**, 24146–24153.

81 M. K. Kesarla, M. O. Fuentez-Torres, M. A. Alcudia-Ramos, F. Ortiz-Chi, C. G. Espinosa-González, M. Aleman, J. G. Torres-Torres and S. Godavarthi, Synthesis of g-C3N4/N-doped CeO_2 composite for photocatalytic degradation of an herbicide, *J. Mater. Res. Technol.*, 2019, **8**, 1628–1635.

82 M. Tahir, B. Tahir, N. A. S. Amin and Z. Y. Zakaria, Photo-induced reduction of CO_2 to CO with hydrogen over plasmonic $Ag\text{-}NPs/TiO_2$ NWs core/shell hetero-junction under UV and visible light, *J. CO2 Util.*, 2017, **18**, 250–260.

83 H. Robatjazi, H. Zhao, D. F. Swearer, N. J. Hogan, L. Zhou, A. Alabastri, M. J. McClain, P. Nordlander and N. J. Halas, Plasmon-induced selective carbon dioxide conversion on earth-abundant aluminum-cuprous oxide antenna-reactor nanoparticles, *Nat. Commun.*, 2017, **8**, 27.

84 S. Ning, H. Xu, Y. Qi, L. Song, Q. Zhang, S. Ouyang and J. Ye, Microstructure Induced Thermodynamic and Kinetic Modulation to Enhance CO_2 Photothermal Reduction: A Case of Atomic-Scale Dispersed Co–N Species Anchored Co@C Hybrid, *ACS Catal.*, 2020, **10**, 4726–4736.

85 A. A. Upadhye, I. Ro, X. Zeng, H. J. Kim, I. Tejedor, M. A. Anderson, J. A. Dumesic and G. W. Huber, Plasmon-enhanced reverse water gas shift reaction over oxide supported Au catalysts, *Catal. Sci. Technol.*, 2015, **5**, 2590–2601.

86 Z. Yang, M. Zeng, K. Wang, X. Yue, X. Chen, W. Dai and X. Fu, Visible light-assisted thermal catalytic reverse water gas reaction over $Cu\text{-}CeO_2$: The synergistic of hot electrons and oxygen vacancies induced by LSPR effect, *Fuel*, 2022, **315**, 123186.

87 H. Zhang, T. Wang, J. Wang, H. Liu, T. D. Dao, M. Li, G. Liu, X. Meng, K. Chang, L. Shi, T. Nagao and J. Ye, Surface-Plasmon-Enhanced Photodriven CO_2 Reduction Catalyzed by Metal–Organic-Framework-Derived Iron Nanoparticles

Encapsulated by Ultrathin Carbon Layers, *Adv. Mater.*, 2016, **28**, 3703–3710.

88 J. Zhao, Q. Yang, R. Shi, I. N. Waterhouse Geoffrey, X. Zhang, W. Li-Zhu, T. Chen-Ho and T. Zhang, FeO–CeO_2 nanocomposites: an efficient and highly selective catalyst system for photothermal CO_2 reduction to CO, *NPG Asia Mater.*, 2020, **12**, 5, DOI: 10.1038/s41427-019-0171-5.

89 X. Wan, Y. Li, Y. Chen, J. Ma, Y.-A. Liu, E.-D. Zhao, Y. Gu, Y. Zhao, Y. Cui, R. Li, D. Liu, R. Long, K. M. Liew and Y. Xiong, A nonmetallic plasmonic catalyst for photothermal CO_2 flow conversion with high activity, selectivity and durability, *Nat. Commun.*, 2024, **15**, 1273.

90 J. Yu, A. Muhetaer, X. Gao, Z. Zhang, Y. Yang, Q. Li, L. Chen, H. Liu and D. Xu, Highly Active Hydrogen-rich Photothermal Reverse Water Gas Shift Reaction on Ni/$LaInO_3$ Perovskite Catalysts with Near-unity Selectivity, *Angew. Chem., Int. Ed.*, 2023, **62**, e202303135.

91 N. Blommaerts, N. Hoeven, D. Arenas Esteban, R. Campos, M. Mertens, R. Borah, A. Glisenti, K. De Wael, S. Bals, S. Lenaerts, S. W. Verbruggen and P. Cool, Tuning the turnover frequency and selectivity of photocatalytic CO_2 reduction to CO and methane using platinum and palladium nanoparticles on Ti-Beta zeolites, *Chem. Eng. J.*, 2021, **410**, 128234.

92 H. Ge, Y. Kuwahara, K. Kusu, H. Kobayashi and H. Yamashita, Enhanced visible-NIR absorption and oxygen vacancy generation of Pt/H_xMoWO_y by H-spillover to facilitate photothermal catalytic CO_2 hydrogenation, *J. Mater. Chem. A*, 2022, **10**, 10854–10864.

93 H. Ge, Y. Kuwahara, K. Kusu and H. Yamashita, Plasmon-induced catalytic CO_2 hydrogenation by a nano-sheet Pt/H_x-MoO_{3-y} hybrid with abundant surface oxygen vacancies, *J. Mater. Chem. A*, 2021, **9**, 13898–13907.

94 Z. Li, Q. Ul Hassan, W. Zhang, L. Zhu, J. Gao, X. Shi, Y. Huang, P. Liu and G. Zhu, Promotion of dual-reaction pathway in CO2 reduction over Pt0/SrTiO3–δ: Experimental and theoretical verification, *Chin. J. Catal.*, 2023, **46**, 113–124.

95 J. Jia, H. Wang, Z. Lu, P. G. O'Brien, M. Ghoussoub, P. Duchesne, Z. Zheng, P. Li, Q. Qiao, L. Wang, A. Gu, A. A. Jelle, Y. Dong, Q. Wang, K. K. Ghuman, T. Wood, C. Qian, Y. Shao, C. Qiu, M. Ye, Y. Zhu, Z.-H. Lu, P. Zhang, A. S. Helmy, C. V. Singh, N. P. Kherani, D. D. Perovic and G. A. Ozin, Photothermal Catalyst Engineering: Hydrogenation of Gaseous CO_2 with High Activity and Tailored Selectivity, *Adv. Sci.*, 2017, **4**, 1700252.

96 J. Jia, P. G. O'Brien, L. He, Q. Qiao, T. Fei, L. M. Reyes, T. E. Burrow, Y. Dong, K. Liao, M. Varela, S. J. Pennycook, M. Hmadeh, A. S. Helmy, N. P. Kherani, D. D. Perovic and G. A. Ozin, Visible and Near-Infrared Photothermal Catalyzed Hydrogenation of Gaseous CO_2 over Nanostructured Pd@Nb_2O_5, *Adv. Sci.*, 2016, **3**, 1600189.

97 Z. Zhu, X. Hu, X. An, M. Xiao, L. Zhang, C. Li and L. He, Photothermal Catalytic CO_2 Hydrogenation with High Activity and Tailored Selectivity Over Monodispersed Pd-Ni Nanoalloys, *Chem. – Asian J.*, 2022, **17**, e202200993.

98 Z. Wu, J. Shen, C. Li, C. Zhang, K. Feng, Z. Wang, X. Wang, D. M. Meira, M. Cai, D. Zhang, S. Wang, M. Chu, J. Chen, Y. Xi, L. Zhang, T.-K. Sham, A. Genest, G. Rupprechter, X. Zhang and L. He, Mo_2TiC_2 MXene-Supported Ru Clusters for Efficient Photothermal Reverse Water–Gas Shift, *ACS Nano*, 2023, **17**, 1550–1559.

99 B. Tahir, M. Tahir and N. A. S. Amin, Photocatalytic CO_2 conversion over Au/TiO_2 nanostructures for dynamic production of clean fuels in a monolith photoreactor, *Clean Technol. Environ. Policy*, 2016, **18**, 2147–2160.

100 X. Zhang, X. Li, D. Zhang, N. Q. Su, W. Yang, H. O. Everitt and J. Liu, Product selectivity in plasmonic photocatalysis for carbon dioxide hydrogenation, *Nat. Commun.*, 2017, **8**, 14542.

101 K. Wang, S. Shao, Y. Liu, M. Cao, J. Yu, C. H. Lau, Y. Zheng and X. Fan, DRIFTS-SSITKA-MS investigations on the mechanism of plasmon preferentially enhanced CO_2 hydrogenation over Au/γ-Al_2O_3, *Appl. Catal., B*, 2023, **328**, 122531.

102 I. Ro, R. Carrasquillo-Flores, J. A. Dumesic and G. W. Huber, Intrinsic kinetics of plasmon-enhanced reverse water gas shift on Au and Au–Mo interfacial sites supported on silica, *Appl. Catal., A*, 2016, **521**, 182–189.

103 B. Lu, F. Quan, Z. Sun, F. Jia and L. Zhang, Photothermal reverse-water-gas-shift over Au/CeO_2 with high yield and selectivity in CO_2 conversion, *Catal. Commun.*, 2019, **129**, 105724.

104 C. Li, Y. Sakata, T. Arai, K. Domen, K.-i. Maruya and T. Onishi, Carbon monoxide and carbon dioxide adsorption on cerium oxide studied by Fourier-transform infrared spectroscopy. Part 1.—Formation of carbonate species on dehydroxylated CeO_2, at room temperature, *J. Chem. Soc., Faraday Trans. 1*, 1989, **85**, 929–943.

105 S. Loridant, Raman spectroscopy as a powerful tool to characterize ceria-based catalysts, *Catal. Today*, 2021, **373**, 98–111.

106 B. Chen, B. Wang, Y. Sun, X. Wang, M. Fu, J. Wu, L. Chen, Y. Tan and D. Ye, Plasma-Assisted Surface Interactions of Pt/CeO_2 Catalyst for Enhanced Toluene Catalytic Oxidation, *Catalysts*, 2019, **9**, 2.

107 R. Schmitt, A. Nenning, O. Kraynis, R. Korobko, A. I. Frenkel, I. Lubomirsky, S. M. Haile and J. L. M. Rupp, A review of defect structure and chemistry in ceria and its solid solutions, *Chem. Soc. Rev.*, 2020, **49**, 554–592.

108 J. Boon, Sorption-enhanced reactions as enablers for CO2 capture and utilisation, *Curr. Opin. Chem. Eng.*, 2023, **40**, 100919.

109 W. Chen, G. Qian, Y. Wan, D. Chen, X. Zhou, W. Yuan and X. Duan, Mesokinetics as a Tool Bridging the Microscopic-to-Macroscopic Transition to Rationalize Catalyst Design, *Acc. Chem. Res.*, 2022, **55**, 3230–3241.

110 W. Chen, W. Fu, X. Duan, B. Chen, G. Qian, R. Si, X. Zhou, W. Yuan and D. Chen, Taming Electrons in Pt/C Catalysts to Boost the Mesokinetics of Hydrogen Production, *Engineering*, 2022, **14**, 124–133.